Evaluation Strategies for the Optimization of Line Source Arrays

Florian Straube[1], Frank Schultz[2], Michael Makarski[3], Sascha Spors[2] and Stefan Weinzierl[1]

[1]*Audio Communication Group, TU Berlin, DE-10587, Berlin, Germany*

[2]*Institute of Communications Engineering, University of Rostock, DE-18119, Rostock, Germany*

[3]*Four Audio GmbH & Co. KG, DE-52134, Herzogenrath, Germany*

Correspondence should be addressed to Florian Straube (`florian.straube@tu-berlin.de`)

ABSTRACT

Line source arrays (LSAs) are used for large scale sound reinforcement, aiming at the synthesis of highly spatial aliasing-free sound fields for the whole audio bandwidth. Numerical optimization of the loudspeakers' driving functions can considerably improve the homogeneity of the intended sound field. In this paper we propose enhanced visualization techniques characterizing the array performance. This may lead to a more convenient interpretation of the LSA radiation behavior. By additionally recommended technical quality measures the LSA design and the optimization requirements might be improved. The approach is exemplarily discussed for fictitious LSA models. Based on a least-mean-square error optimization using a loudspeaker weight energy constraint, the driving functions are derived. It is shown by means of the visualizations and measures why this optimization scheme being common practice in sound field synthesis applications is inappropriate for the problem at hand and that spatial aliasing has a large impact on the synthesized sound fields. We recommend to incorporate the proposed quality measures as criteria for future optimization approaches.

1. INTRODUCTION

Optimized electronic control of curved line source arrays (LSAs) for improved sound reinforcement has gained interest in the last two decades. The calculation of appropriate driving signals, i.e. FIR filters for the individual LSA loudspeakers in order to generate a desired sound field by numerical optimization techniques was discussed in [1–7]. These approaches yield considerable improvements with respect to homogeneous audience coverage and/or avoidance of high side lobe energy compared to manually adjusted setups.

It is common practice to select control positions which the sound field is to be optimized at in the vertical LSA radiation plane (here the *xy*-plane), thus assuming that horizontal radiation is homogeneous. The control positions may include audience (target) and non-audience (avoid) zones, cf. [1, Fig. 17], [3, Fig. 1], [4, Fig. 2], [5, Fig. 1], [6, Fig. 4], [7, Fig. 3]. Typically the predicted sound field is either visualized as the sound pressure level (SPL) over the whole *xy*-plane for single frequencies or frequency bands (e. g. MAPP Online Pro [8], EASE Focus, [4, Fig. 3]) or given as a so called position index plot (also termed positional map), where the SPL spectra for certain evaluated positions (mainly the control positions) within the *xy*-plane are depicted [6, Fig. 5], [3, Fig. 2]. Recent software also include plots of the SPL distribution on 3D audience surfaces, e. g. EAW Resolution 2, EASE Focus 2.

In some papers the resulting LSA far-field radiation pattern is given as frequency dependent polar plots or isobar plots [1, 6]. To the authors' knowledge, this is not supported by any prediction software so far. Furthermore, a spectral deviation measure, as discussed in [6], is not yet incorporated into commercial software.

The resulting driving functions for the individual loudspeakers, typically realized with FIR-filters, are rarely documented except in [2]. Hence, a valid judgment of the approaches' feasibility in terms of the electrical load and load balancing is not possible.

In this contribution, we aim at an enhanced visual treatment of the data that may be helpful for an improved interpretation of the sound fields generated by LSAs.

This includes the SPL distribution over space for frequency bands (SPLxy), the frequency responses for all audience positions (FAP), the position index plot (PIP), the far-field radiation pattern (FRP) as an isobar plot and the driving function index plot (DFIP) as magnitude and group delay spectra and/ or impulse responses for the individual loudspeakers. Each visualization exhibits advantages and disadvantages for the interpretation of the occurring phenomena. Therefore, the different graphics should be presented and discussed in combination.

A complex-directivity point source model (CDPS) [9] of a curved LSA, commonly used for sound field prediction, is generated from ideally baffled pistons for our discussion. This modeling may not properly represent practical LSAs with respect to low frequencies and rearward radiation but it allows to design reproducible LSA setups with a convenient parametrization. Two models of LSA cabinets are used. They differ in the number of the individual drivers per cabinet in the mid and high frequency section. Thus, we follow [7] demonstrating improved optimization by increasing the driving granularity of the LSA in order to reduce spatial aliasing. LSA designs that are compliant to the initial Wavefront Sculpture Technology (WST) [10] or behave similarly feature rather large waveguides. Their capability of pure electronic beam steering without producing spatial aliasing is therefore limited for the highest audio frequencies [8]. These LSAs have to be adapted to the listener region by geometrical curving, additionally to the electronic control. Different spatial aliasing effects are investigated for the two LSA designs that can be conveniently discussed by means of the proposed visualization and measures.

The paper is organized as follows: In Sec. 2 the chosen LSA models and the venue under evaluation are given. The CDPS model and further mathematical fundamentals are shortly revisited in Sec. 3. The selected optimization algorithm solving the inverse problem is discussed in Sec. 4. The proposed visualizations and measures for the optimized LSAs are introduced in Sec. 5 and discussed in Sec. 6.

2. SETUP

A curved LSA setup is examined for a common concert venue following a practical example presented in [5, Ch. 6.1]: a multi-stand arena with audience and non-audience sections given within the *xy*-plane.

2.1. LSA Setup

The LSA setup and the geometry under discussion is schematically depicted in Fig. 1. A total number of

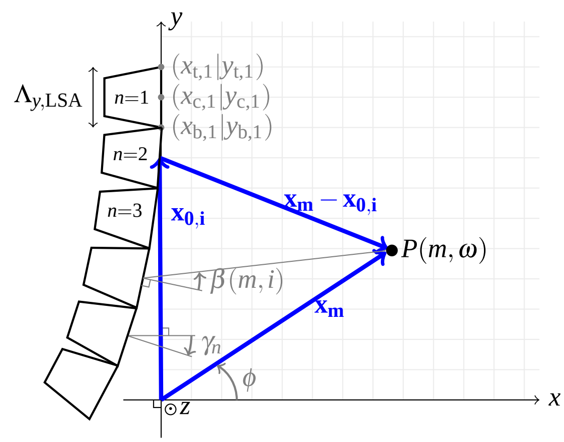

Fig. 1: Sketch of the LSA setup under discussion. A total of $N = 16$ LSA cabinets of the height $\Lambda_{y,\mathrm{LSA}} = 0.372\,\mathrm{m}$ is used. See Tab. 6 for exact positions.

$N = 16$ LSA cabinets with $n = 1,2,\ldots,N$ is used. $\Lambda_{y,\mathrm{LSA}}$ denotes the front grille's height of a single LSA cabinet, chosen to $\Lambda_{y,\mathrm{LSA}} = 0.372\,\mathrm{m}$ resulting in an overall LSA length of ≈5.95 m. The front grille top and bottom coordinates $(x_\mathrm{t}, y_\mathrm{t})$ and $(x_\mathrm{b}, y_\mathrm{b})$ resp. of the individual cabinets are given as

$$\begin{pmatrix} x_{\mathrm{t},n} \\ y_{\mathrm{t},n} \end{pmatrix} = \begin{pmatrix} x_\mathrm{H} \\ y_\mathrm{H} \end{pmatrix} - \sum_{\mu=1}^{\mu=n-1} \Lambda_{y,\mathrm{LSA}} \begin{pmatrix} \sin\gamma_\mu \\ \cos\gamma_\mu \end{pmatrix}, \quad (1)$$

$$\begin{pmatrix} x_{\mathrm{b},n} \\ y_{\mathrm{b},n} \end{pmatrix} = \begin{pmatrix} x_\mathrm{H} \\ y_\mathrm{H} \end{pmatrix} - \sum_{\mu=1}^{\mu=n} \Lambda_{y,\mathrm{LSA}} \begin{pmatrix} \sin\gamma_\mu \\ \cos\gamma_\mu \end{pmatrix}, \quad (2)$$

using $x_\mathrm{H} = 0\,\mathrm{m}$ and $y_\mathrm{H} = 3\,\mathrm{m}$ as the initial front grille top position of the top LSA cabinet ($n = 1$) and the individual tilting angles γ_n. The tilting angles were set according to the intended audience coverage and are compliant to the 5$^{\mathrm{th}}$ WST criterion [10, p. 929]. The arrays' physical opening angle amounts to about 41°. In Tab. 5 in the Appendix, the chosen tilting angles γ_n and the resulting front grille center positions $(x_{\mathrm{c},n}, y_{\mathrm{c},n})$ are listed.

The LSA is built from multi-way cabinets, each modeled with L_LF, L_MF, L_HF vertically stacked, individually controlled drivers for the low, mid and high frequency band (LF, MF, HF). With (1) and (2) the front grille center position of the i-th LSA driver is given as

$$\mathbf{x_{0,i}} = \begin{pmatrix} x_{0,i} \\ y_{0,i} \end{pmatrix} = \begin{pmatrix} x_{\mathrm{t},n} \\ y_{\mathrm{t},n} \end{pmatrix} + \frac{l-0.5}{L} \begin{pmatrix} x_{\mathrm{b},n} - x_{\mathrm{t},n} \\ y_{\mathrm{b},n} - y_{\mathrm{t},n} \end{pmatrix}, \quad (3)$$

using $l = 1,2,\ldots,L$ and $i = (n-1)\cdot L + l$ for $L = \{L_{\mathrm{LF}}, L_{\mathrm{MF}}, L_{\mathrm{HF}}\}$ with respect to the different frequency bands. We have exemplarily chosen two LSA cabinet designs

$$\mathrm{LSA}_1 = \begin{cases} L_{\mathrm{LF}} = 1 \\ L_{\mathrm{MF}} = 2 \\ L_{\mathrm{HF}} = 1 \end{cases} \quad \mathrm{LSA}_2 = \begin{cases} L_{\mathrm{LF}} = 1 \\ L_{\mathrm{MF}} = 4 \\ L_{\mathrm{HF}} = 10 \end{cases},$$

deploying the circular piston model (8) for LF and MF and the line piston model (9) for HF as well as ideal crossover filters (brick wall) with the frequencies $f_{\mathrm{LF,MF}} = 400\,\mathrm{Hz}$ and $f_{\mathrm{MF,HF}} = 1.5\,\mathrm{kHz}$. The Active Radiating Factor (ARF) [10, Ch. 3.2] is used to specify the piston dimensions – i.e. the circular piston radius R and the line piston length Λ_y – related to the fixed distance between adjacent piston centers (discretization)

$$\Delta y = \frac{\Lambda_{y,\mathrm{LSA}}}{L}. \tag{4}$$

The ARF of a line piston reads [11, (21)], [10, Sec. 3.2]

$$\mathrm{ARF}_{\mathrm{line}} = \alpha = \frac{\Lambda_y}{\Delta y} \qquad 0 \le \alpha \le 1, \tag{5}$$

and the ARF for a circular piston can be written as [11, (26,27)]

$$\mathrm{ARF}_{\mathrm{circ}} = \frac{\pi}{4}\alpha^2 = \frac{\pi}{4}\left(\frac{2R}{\Delta y}\right)^2 \qquad 0 \le \alpha \le 1. \tag{6}$$

Note that $\mathrm{ARF}_{\mathrm{circ}}$ is in fact a ratio of surface areas ($\mathrm{ARF}_{\mathrm{circ}} \neq \alpha$), whereas a ratio of line lengths is defined for the line piston ($\mathrm{ARF}_{\mathrm{line}} = \alpha$). We use $\alpha = 0.82$ for both the line and the circular piston, consequently fulfilling the first WST criterion for line pistons (cf. [10, p. 917], [11]). The piston dimensions $\{\Lambda_y, 2R\}$ and

L	Δy/cm	Δy/in	$\{\Lambda_y, 2R\}$/cm	$\{\Lambda_y, 2R\}$/in
1	37.2	14.65	30.5	12
2	18.6	7.32	15.25	6
4	9.3	3.66	7.63	3
10	3.72	1.46	3.05	1.2

Table 1: Relation between the number L of employed pistons per LSA cabinet, the discretization Δy (distance between adjacent pistons centers) and the piston dimensions: diameter $2R$ or length Λ_y for $\alpha = 0.82$.

Freq	L	f_{alias}/Hz	$\{\Lambda_y, 2R\}$/in	$\mathrm{dB}_{\mathrm{SPL@1W,1m}}$
$\mathrm{LF}_{1,2}$	1	461	12 (circ)	96
MF_1	2	922	6 (circ)	94
MF_2	4	1844	3 (circ)	86
HF_1	1	461	12 (line)	112
HF_2	10	4610	1.2 (line)	112

Table 2: Piston dimensions $\{\Lambda_y, 2R\}$ and assumed sensitivities $\mathrm{dB}_{\mathrm{SPL@1W,1m}}$ for LSA_1 and LSA_2 (separately for the different frequency bands and with L drivers per cabinet). The aliasing frequency f_{alias} refers to the spatial sampling condition $\Delta y \le \frac{c}{2f}$ for straight arrays.

the piston center distances Δy for the two LSA cabinets are listed in Tab. 1. Table 2 indicates the assumed loudspeaker sensitivities and the expected aliasing frequencies for straight arrays that may differ slightly from these of curved arrays. The LSA_1 models a typical WST-compliant array of the first generation, whereas the LSA_2 model with a larger number of individual pistons in the MF and HF band is comparable with some recent array designs.

2.2. Venue Geometry

A multi-stand arena with audience and non-audience sections, i.e. zones to be covered and zones to be avoided, is modeled by a two dimensional slice representation. The xy-plane only is considered for vertical radiation, cf. Fig. 2. This is a common approach for optimiza-

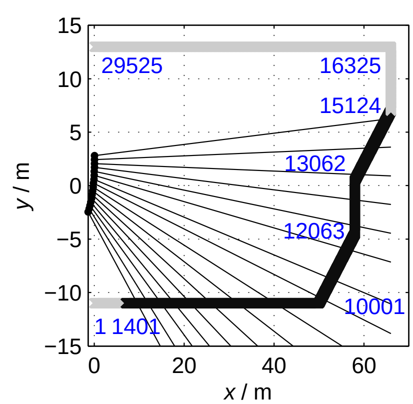

Fig. 2: Venue slice within the xy-plane with audience (black) as well as non-audience/ avoid (gray) zones and selected index numbers from M receiver positions.

tion schemes, cf. [1–7,12]. $M = 29\,525$ receiver positions with $m = 1,2,...,M$ are taken into account. This corresponds to a distance of 0.005 m between the receiver positions ensuring a discretization which approximately equals one fourth of the wave length at 17.2 kHz. The receiver positions are composed of M_a audience positions from the set $\mathscr{M}_\mathrm{a}$ and M_na non-audience positions from the set $\mathscr{M}_\mathrm{na}$ which $M = M_\mathrm{a} + M_\mathrm{na}$ holds for. They are characterized by the position vectors $\mathbf{x_m} = (x_m, y_m, 0)^\mathrm{T}$ and are numbered counterclockwise starting from the position under the LSA that is the closest one to the LSA (index 1, cf. Fig. 2). The venue slice coordinates are documented in Tab. 6 in the Appendix.

Note that the terms *bright zone* and *dark zone* used in the field of multi-zone sound field synthesis (MZSFS) [13–18] correspond to the audience zone and the non-audience zone used in the field of sound reinforcement.

3. CDPS MODEL

The sound field prediction is based on the complex-directivity point source model of baffled piston far-field radiation patterns. Using the $\mathrm{e}^{+\mathrm{j}\omega t}$ time convention it reads [19, (5)], [1, (3-5)], [20, Sec. 1.1], [9, (11)]

$$P(m,\omega) = \sum_{i=1}^{i=LN} D(i,\omega) \times \underbrace{H_\mathrm{post}(\beta(m,i),\omega) \cdot \frac{\mathrm{e}^{-\mathrm{j}\frac{\omega}{c}|\mathbf{x_m}-\mathbf{x_{0,i}}|}}{4\pi|\mathbf{x_m}-\mathbf{x_{0,i}}|} \cdot \frac{\Lambda_{y,\mathrm{LSA}}}{L}}_{G(m,i,\omega)}. \quad (7)$$

Air is assumed to be homogeneous and dissipation-less with a constant speed of sound $c = 343\,\mathrm{m/s}$. $P(m,\omega)$ denotes the sound pressure spectrum at the receiver position $\mathbf{x_m}$ with $[P(m,\omega)] = 1\,\mathrm{Pa/Hz}$. The complex driving function spectrum $D(i,\omega)$ with $[D(i,\omega)] = 1\,\mathrm{Pa/Hz}$ of the i-th source is directly proportional to the source's velocity spectrum. Terming the acoustic transfer function (ATF) from the i-th source to the receiver positions, $G(m,i,\omega)$ is composed of the free-field 3D Green's function $\frac{\mathrm{e}^{-\mathrm{j}\frac{\omega}{c}|\mathbf{x_m}-\mathbf{x_{0,i}}|}}{4\pi|\mathbf{x_m}-\mathbf{x_{0,i}}|}$ (i.e. the ideal point source), a specific far-field radiation pattern $H_\mathrm{post}(\beta(m,i),\omega)$ and the distance $\Delta y = \Lambda_{y,\mathrm{LSA}}/L$ between adjacent piston centers (discretization) for L sources per LSA cabinet. The index *post* refers to the spatial lowpass postfilter characteristics of the speakers within the spatial sampling model, cf. [21]. In the remainder the notation of the dependence $\beta(m,i)$ is omitted.

The far-field radiation pattern of the baffled circular piston with a constant surface velocity is [22, (26.42)]

$$H_\mathrm{post,circ}(\beta,\omega) = \frac{2J_1\left(\frac{\omega}{c}R\sin\beta\right)}{\frac{\omega}{c}R\sin\beta}, \quad (8)$$

denoting the cylindrical Bessel function of 1st kind of 1st order as $J_1(\cdot)$ [23, (10.2.2)]. The line piston models an ideal waveguide for the HF band and its far-field radiation pattern can be written as [22, (26.44)]

$$H_\mathrm{post,line}(\beta,\omega) = \frac{\sin\left(\frac{\omega}{c}\frac{\Lambda_y}{2}\sin\beta\right)}{\frac{\omega}{c}\frac{\Lambda_y}{2}\sin\beta}. \quad (9)$$

Note that these patterns exhibit main lobe unity gain in order to control the energy radiated by the pistons via the assumed sensitivities.

This modeling was also approached in [4, 19]. The model certainly has some drawbacks, such as (i) the infinite, straight baffle assumption, (ii) the constant diaphragm's velocity assumption and (iii) no valid rearward and low-frequency prediction. BEM-based models and measured LSA cabinet data [7, 20] provide results that closer match the reality. However, since we are mainly interested in different visualization methods and measures, the baffled piston model is sufficiently precise, especially for demonstrating spatial aliasing phenomena for high audio frequencies. Note that (7) correctly synthesizes the Fresnel (chaotic) and collective Fraunhofer region [24, Fig. 16] of the whole array if the respective receiver position is located in the far-field of the individual pistons [9, 11]. This does not impose any practical limitations as the audience is typically located in some meters distance from individual LSA cabinets.

4. OPTIMIZATION

For the application of optimization algorithms, (7) is transformed to matrix notation accounting for all receiver positions M for a single frequency (cf. [5, (1)], [4, (1)])

$$\mathbf{p}(\omega) = \mathbf{G}(\omega)\,\mathbf{d}(\omega) \quad (10)$$

with $\mathbf{p}(\omega)$ denoting the $(M \times 1)$ vector of sound pressure spectra at all considered positions $\mathbf{x_m}$, $\mathbf{G}(\omega)$ denoting the $(M \times LN)$ ATF matrix and $\mathbf{d}(\omega)$ denoting the $(LN \times 1)$ vector of the complex driving weights per angular frequency ω at all source positions $\mathbf{x_{0,i}}$. Then, for a desired sound field at the evaluation positions $\mathbf{x_m}$,

$$\mathbf{p}_\mathrm{des}(\omega) = \mathbf{G}(\omega)\,\mathbf{d}(\omega) \quad (11)$$

has to be solved for the loudspeaker driving weights $\mathbf{d}(\omega)$. Since $M > LN$, i.e. the number of evaluation positions is larger than the number of individual sources, an ill-posed inverse problem must be analyzed [25–27]. In this paper, we use a least-mean-square (LMS) optimization method with Tikhonov regularization imposing an energy constraint on the loudspeaker weights [28]. This is often used for numerical sound field synthesis applications. The optimization is performed separately for each frequency.

The desired sound field $\mathbf{p}_{\mathrm{des}}(\omega)$ in principle could be set arbitrarily. However, the used array geometry restricts the choice to physically realizable sound fields. Typically a desired level decay over the audience zone and a level offset for the avoid zone can be defined in practical realizations [3]. We have chosen

$$P_{\mathrm{des,3\ dB}}(m,\omega) \propto \frac{\mathrm{e}^{-\mathrm{j}\frac{\omega}{c}|\mathbf{x_m}-\mathbf{x_S}|}}{\sqrt{|\mathbf{x_m}-\mathbf{x_S}|}} \tag{12}$$

as the target function for the optimization. We thus aim at a desired sound field that complies with a sound field generated by a virtual line monopole at the position $\mathbf{x_S}$ deploying the large argument-approximation of the 2D Green's function and simultaneously ignoring the temporal lowpass characteristics and the frequency independent $\pi/4$-phase shift [29, (26)]. The source position is chosen to

$$\mathbf{x_S} = \frac{1}{2}\left[\begin{pmatrix} x_{\mathrm{t},1} \\ y_{\mathrm{t},1}\end{pmatrix} + \begin{pmatrix} x_{\mathrm{b},16} \\ y_{\mathrm{b},16}\end{pmatrix}\right] = \begin{pmatrix} -0.7537\,\mathrm{m} \\ 0.1938\,\mathrm{m}\end{pmatrix}, \tag{13}$$

ensuring that the origin of the virtual line source is located behind the LSA. A target sound pressure level of 100 $\mathrm{dB_{SPL}}$ at the first receiver position (index 1401) within the audience zone was chosen. For the avoid zone we require a level decrease of 20 dB compared to the audience zone using a smooth dB-transition between audience and non-audience zones.

In [28] the LMS optimization with Tikhonov regularization of the loudspeakers' driving functions is termed loudspeaker weight energy (LWE) according to the considered constraint. In order to solve (11) w.r.t. the loudspeaker weights, the objective function to be minimized reads

$$\begin{aligned} &\min_{\mathbf{d}(\omega)} \|\mathbf{G}(\omega)\mathbf{d}(\omega) - \mathbf{p}_{\mathrm{des}}(\omega)\|_2^2 \\ &\text{subject to:} \quad \|\mathbf{d}(\omega)\|_2^2 \leq D_{\max}^2 \end{aligned} \tag{14}$$

denoting the squared Euclidean norm $\|\cdot\|_2^2$ [23, (3.2.13)] and the constraint $D_{\max}^2$ as the limit for the summed squares of the driving functions' absolute values (cf. [28, (1)]). The solution is well known as

$$\mathbf{d}(\omega,\lambda_{\mathrm{reg}}) = [\mathbf{G}(\omega)^{\mathrm{H}}\mathbf{G}(\omega) + \lambda_{\mathrm{reg}}\mathbf{I}_{LN}]^{-1}\,\mathbf{G}(\omega)^{\mathrm{H}}\mathbf{p}_{\mathrm{des}}(\omega), \tag{15}$$

with the regularization parameter λ_{reg}. Taking $D_{\max}^2$ into account, λ_{reg} can be found by means of singular value analysis and using the Newton's method, cf. [28, Sec. II. B/C]. The Hermitian, i.e. the conjugate transpose, is denoted by $^{\mathrm{H}}$ and $\mathbf{I}_{LN}$ is the $(LN \times LN)$ identity matrix. Note that this approach does not allow for the limitation of the maximum tolerated electric power of the individual sources. Therefore, the resulting loads of the individual drivers must be carefully monitored. This is one significant drawback of the LWE algorithm. Other approaches were discussed in literature that are presumably better suited for LSA optimization [1, 3, 5].

5. EVALUATION

In this section the proposed visualizations and measures are introduced by means of optimization examples for the two fictitious LSAs. The optimizations were performed for a logarithmically spaced frequency vector with $f_{\mathrm{start}} = 200\,\mathrm{Hz}$, $f_{\mathrm{stop}} = 20\,\mathrm{kHz}$ and $1/36$ octave resolution. In Fig. 11 in the Appendix the optimization parameters are depicted.

5.1. Graphical Representation

The position index plots (PIPs) and the far-field radiation patterns (FRPs) over frequency as well as an overlay of all frequency responses for the audience positions (FAP) are depicted in Fig. 3. Using the indexing of Fig. 2 the PIP shows the resulting SPL spectra at all control positions $\mathbf{x_m}$. The frequency response within the audience zone should ideally be as linear as possible following the desired level decay resulting from the different distances to the virtual line source (12). In the avoid zone the desired SPL reduction should ideally be met. The widespread method of optimizing sound fields for selected positions in a venue slice bears the risk of neglecting the sound field that was excluded from optimization, i.e. positions that are not part of PIP. It is thus important to offer further visualizations. The FRP represents the polar patterns for radiating angles $|\phi| \leq 90°$ as an isobar plot over all evaluated frequencies. It conveniently indicates strong side lobes (from windowing, i.e. because of the finite length of the LSA) and grating lobes (from spatial aliasing, i.e. because of the distance between adjacent drivers) that should be avoided to obtain a homogeneous audience coverage as well as low

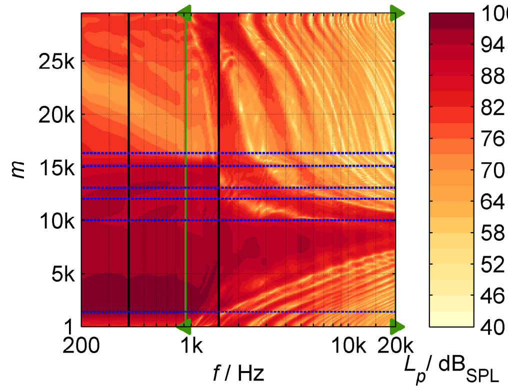

(a) PIP LSA_1

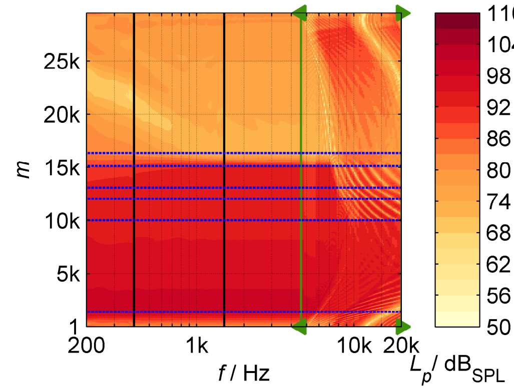

(b) PIP LSA_2

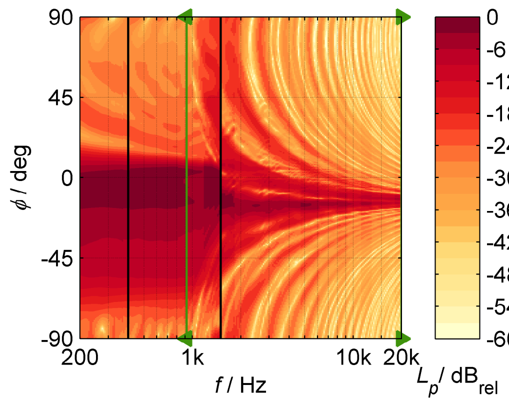

(c) FRP LSA_1

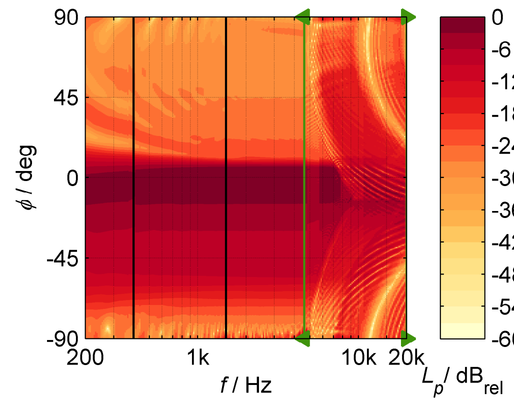

(d) FRP LSA_2

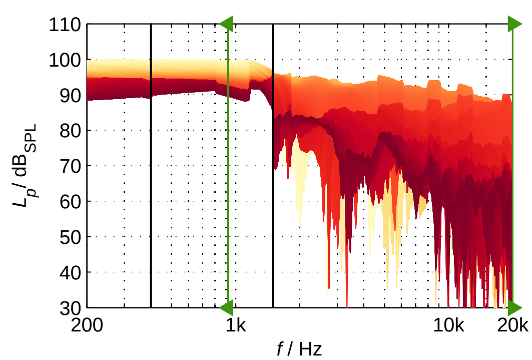

(e) FAP LSA_1

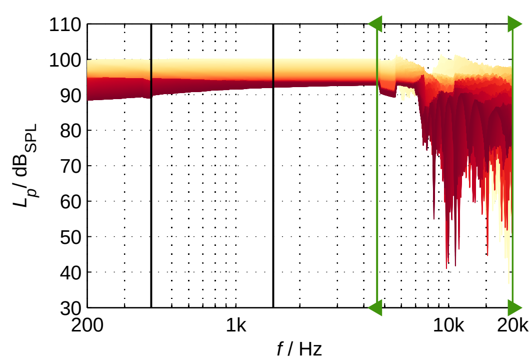

(f) FAP LSA_2

Fig. 3: Position index plot (PIP), far-field radiation pattern (FRP) and frequency responses for all audience positions (FAP) for the LSA_1 (left) and the LSA_2 (right). In the FAP the color transition from yellow to red corresponds to the transition of the positions close to the LSA to the positions far from the LSA. The crossover frequencies (black) and the spatial aliasing frequencies of straight arrays (green with arrows) according to Tab. 2 are charted for orientation.

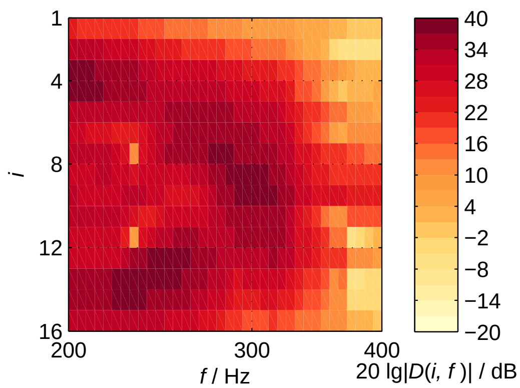

(a) DFIP (magnitudes) for LF

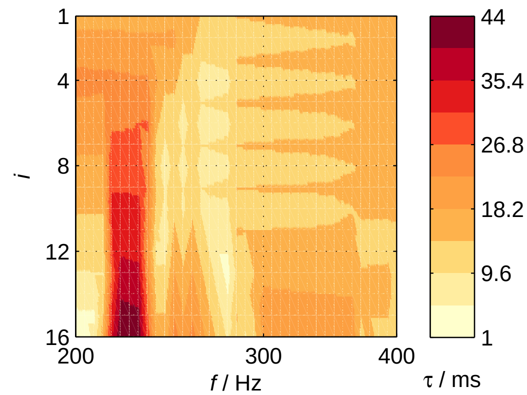

(b) DFIP (delays) for LF

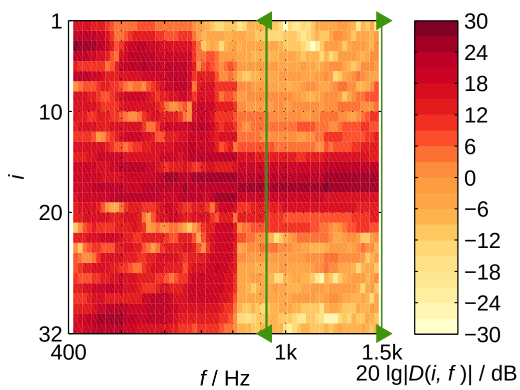

(c) DFIP (magnitudes) for MF

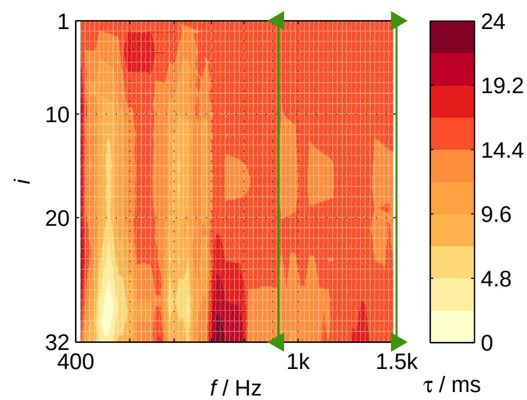

(d) DFIP (delays) for MF

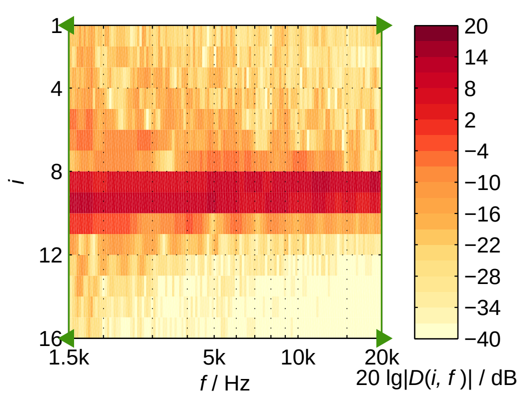

(e) DFIP (magnitudes) for HF

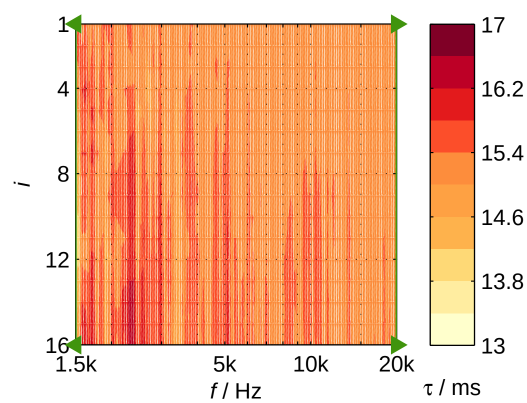

(f) DFIP (delays) for HF

Fig. 4: Driving Function Index Plots (DFIPs) over frequency f and source number i for the LWE-optimized LSA_1. Magnitudes and delays are visualized separately for the low (LF), mid (MF) and high (HF) frequency range. The spatial aliasing frequencies of straight arrays (green with arrows) according to Tab. 2 are charted for orientation.

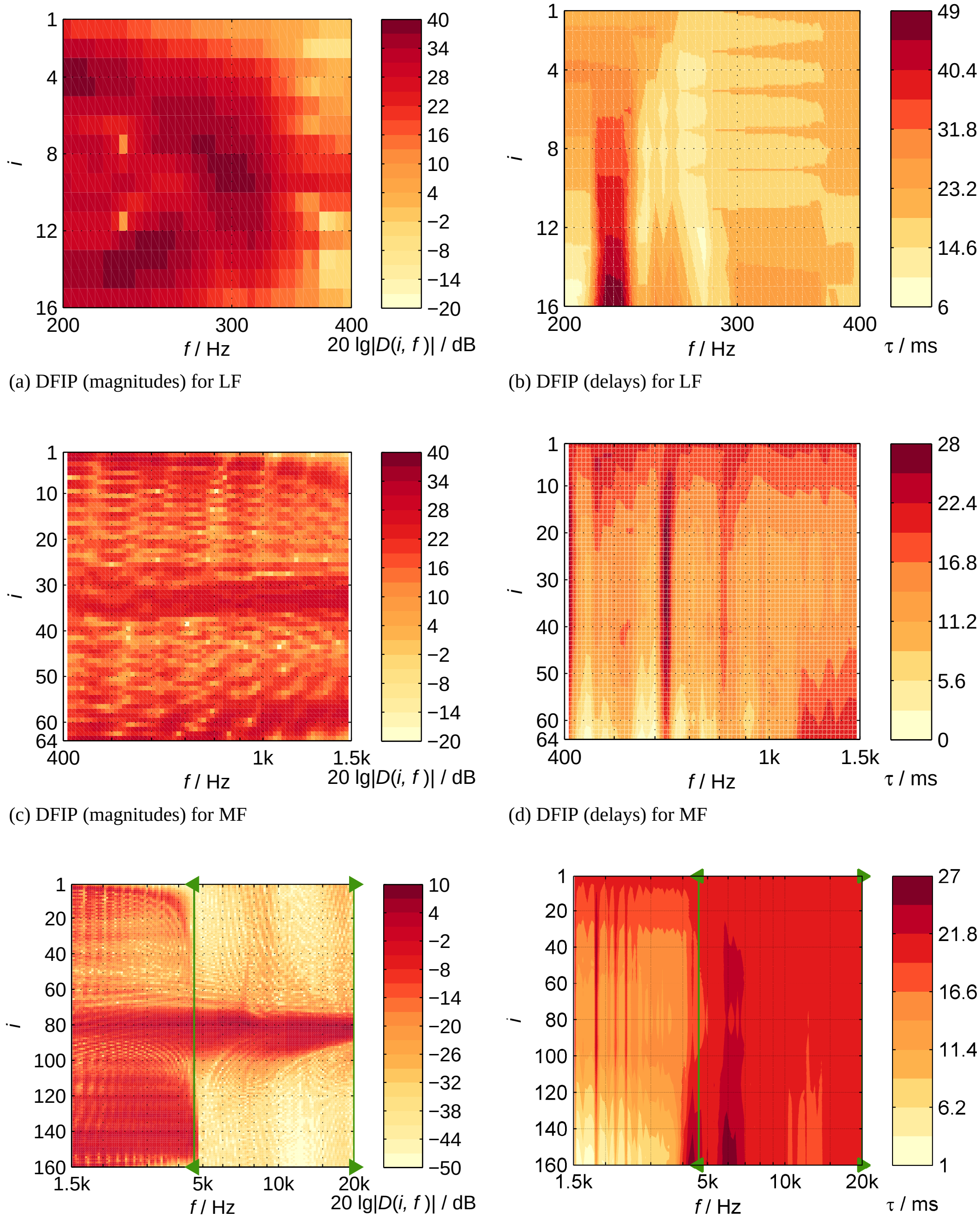

(a) DFIP (magnitudes) for LF

(b) DFIP (delays) for LF

(c) DFIP (magnitudes) for MF

(d) DFIP (delays) for MF

(e) DFIP (magnitudes) for HF

(f) DFIP (delays) for HF

Fig. 5: Driving Function Index Plots (DFIPs) over frequency f and source number i for the LWE-optimized LSA_2. Magnitudes and delays are visualized separately for the low (LF), mid (MF) and high (HF) frequency range. The spatial aliasing frequencies of straight arrays (green with arrows) according to Tab. 2 are charted for orientation.

short name	item	variable	parameters
PIP	position index plot	sound pressure level L_p	frequency f, position index m
FRP	far-field radiation pattern	sound pressure level L_p	frequency f, vertical angle ϕ
FAP	frequency responses of all audience positions	sound pressure level L_p	frequency f
SPLxy	sound pressure levels in the xy-plane	sound pressure level L_p	coordinates x, y
DFIP	driving function index plot	magnitudes and phases (as delay τ) of the driving functions $D(i, \omega)$	frequency f, driver index i

Table 3: Overview of the proposed visualizations.

SPLs within the avoid zones. This cannot necessarily be seen in the PIP. Illustrating the SPLs for the evaluated *xy*-plane and specified frequencies or frequency bands is another common approach to evaluate the radiation characteristics. For specified frequencies this can be viewed in the SPLxy plots (Fig. 9 and Fig. 10 in the Appendix) for both LSAs under discussion. While giving a fast overview of the coverage and the side and the grating lobes at those frequencies, the obtained SPL spectra for the intended listener and avoid positions are not easily accessible. Hence, all four visualizations (PIP, FRP, FAP, SPLxy) should be provided in combination for convenient interpretation.

The driving function index plots (DFIP) are depicted individually for the LF, MF and HF band in Fig. 4 for the LSA_1 and in Fig. 5 for the LSA_2. They represent the magnitudes and group delays over frequency that have to be applied to the individual sources i in order to obtain the optimized sound field. On the one hand the load and the load balancing of the drivers can be evaluated by the magnitude plot, on the other hand the required FIR filter length can be estimated by the delay plot. An overview of the proposed visualizations can be found in Tab. 3.

5.2. Technical Quality Measures

In sound field synthesis applications either the frequency dependent absolute error of (14) or the position and frequency dependent relative error

$$\varepsilon_{\text{abs}}(\omega) = \|\mathbf{G}(\omega)\mathbf{d}(\omega) - \mathbf{p}_{\text{des}}(\omega)\|_2^2, \qquad (16)$$

$$\varepsilon_{\text{rel}}(m,\omega) = \left|\frac{P_{\text{des}}(m,\omega) - P(m,\omega)}{P_{\text{des}}(m,\omega)}\right|^2, \qquad (17)$$

resp. are typically evaluated to rate the obtained sound field's technical quality. We propose two further measures using the magnitudes of the sound pressure that might deliver additional insights. The first frequency dependent measure relates the obtained average levels of the audience zone and the non-audience zone

$$L_{p,\text{a,na}}(\omega) = 10\log_{10}\left(\frac{\frac{1}{M_\text{a}}\|\mathbf{p}_{m\in\mathscr{M}_\text{a}}(\omega)\|_2^2}{\frac{1}{M_\text{na}}\|\mathbf{p}_{m\in\mathscr{M}_\text{na}}(\omega)\|_2^2}\right), \qquad (18)$$

that is depicted in Fig. 6a and Fig. 6b for the two LWE-optimized LSAs. This measure corresponds to the acoustic contrast [13, (16)], [15, (2)], [16, (2)] established in MZSFS. It allows for a direct judgment of the energy steering but might be misleading if the audience coverage is insufficient due to spatial aliasing.

Furthermore, we recommend to deploy the frequency dependent distribution measure

$$L_{p,\text{des,opt},q}(\omega) = \underset{m}{\mathscr{Q}_q}\left[10\log_{10}\left(\frac{|P_{\text{des}}(m,\omega)|^2}{|P(m,\omega)|^2}\right)\right] \qquad (19)$$

using the operator $\underset{m}{\mathscr{Q}_q}[\cdot]$ to calculate the $q = \{0.05,\ 0.25,\ 0.5,\ 0.75,\ 0.95\}$ quantiles of the level difference between the desired and the obtained sound field over all receiver positions $\mathbf{x_m}$ in this particular case. This can be viewed in Fig. 6c and Fig. 6d. When the obtained sound field $|\mathbf{p}(\omega)|$ conforms very well to the desired one $|\mathbf{p}_{\text{des}}(\omega)|$, the measure should provide a median (i.e. the 0.5-quantile) near 0 dB and very little spread in the other quantiles. In contrast to the errors in (16) and (17), $L_{p,\text{des,opt},q}(\omega)$ additionally provides the spread of the deviations and disregards the effect of phase differences between the desired and the obtained sound field.

To receive further impressions of the required power and load balancing (LB) necessary for producing the sound fields, the following source related distribution measures may be useful. They are in line with the con-

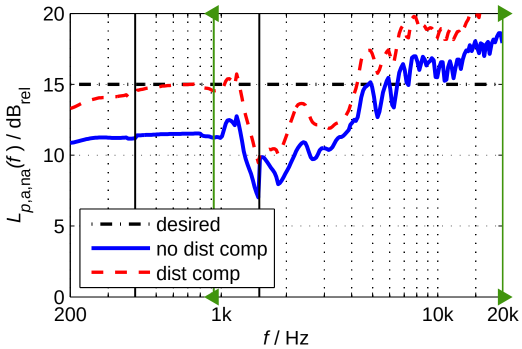

(a) $L_{p,\mathrm{a,na}}(\omega)$

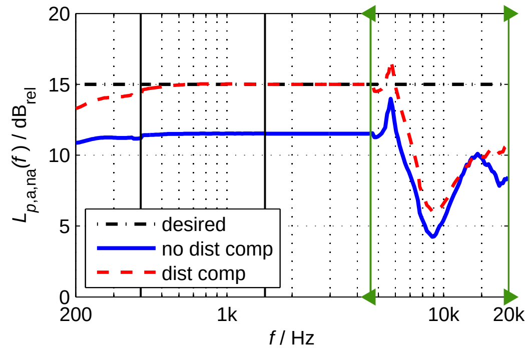

(b) $L_{p,\mathrm{a,na}}(\omega)$

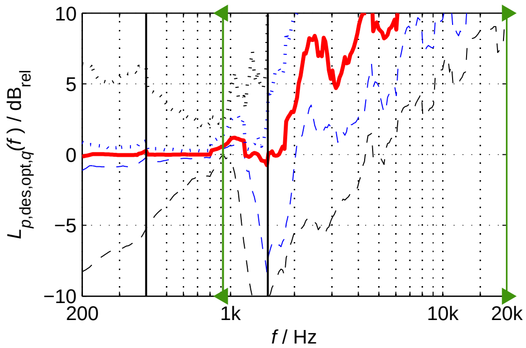

(c) $L_{p,\mathrm{des,opt},q}(\omega)$

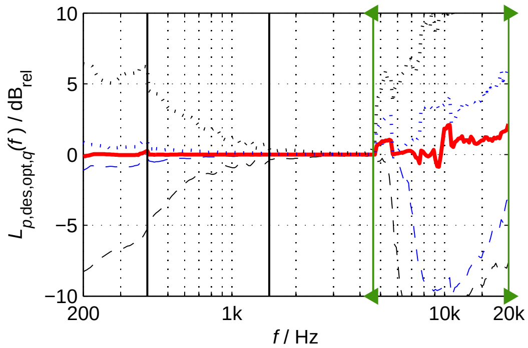

(d) $L_{p,\mathrm{des,opt},q}(\omega)$

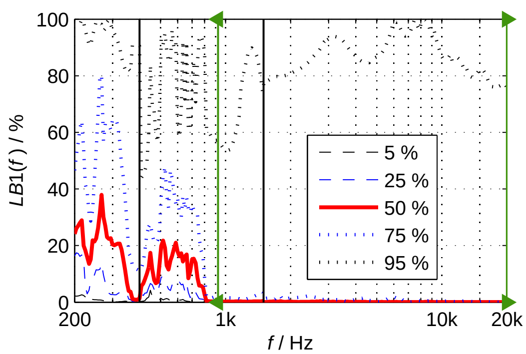

(e) $LB1(\omega)$

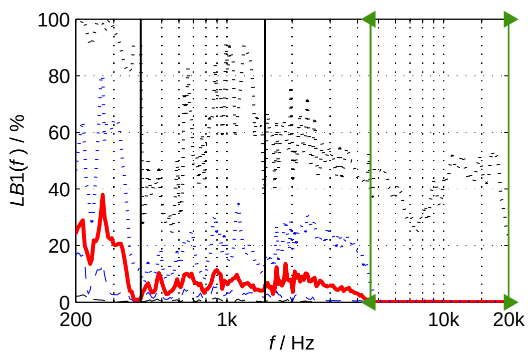

(f) $LB1(\omega)$

Fig. 6: Evaluation plots for the LSA$_1$ (left) and the LSA$_2$ (right), top: relation of the obtained average levels of the audience and the non-audience zone $L_{p,\mathrm{a,na}}(\omega)$, eq. (18) – the desired relation, the relation without distance compensation, and with distance compensation, i.e. compensation of the level decay, mid: frequency dependent distribution measure $L_{p,\mathrm{des,opt},q}(\omega)$, eq. (19), bottom: frequency dependent load balancing $LB1(\omega)$ of the drivers, eq. (20). Note that the legend in (e) is valid for all depicted distribution measures. The crossover frequencies (black) and the spatial aliasing frequencies of straight arrays (green with arrows) according to Tab. 2 are charted for orientation.

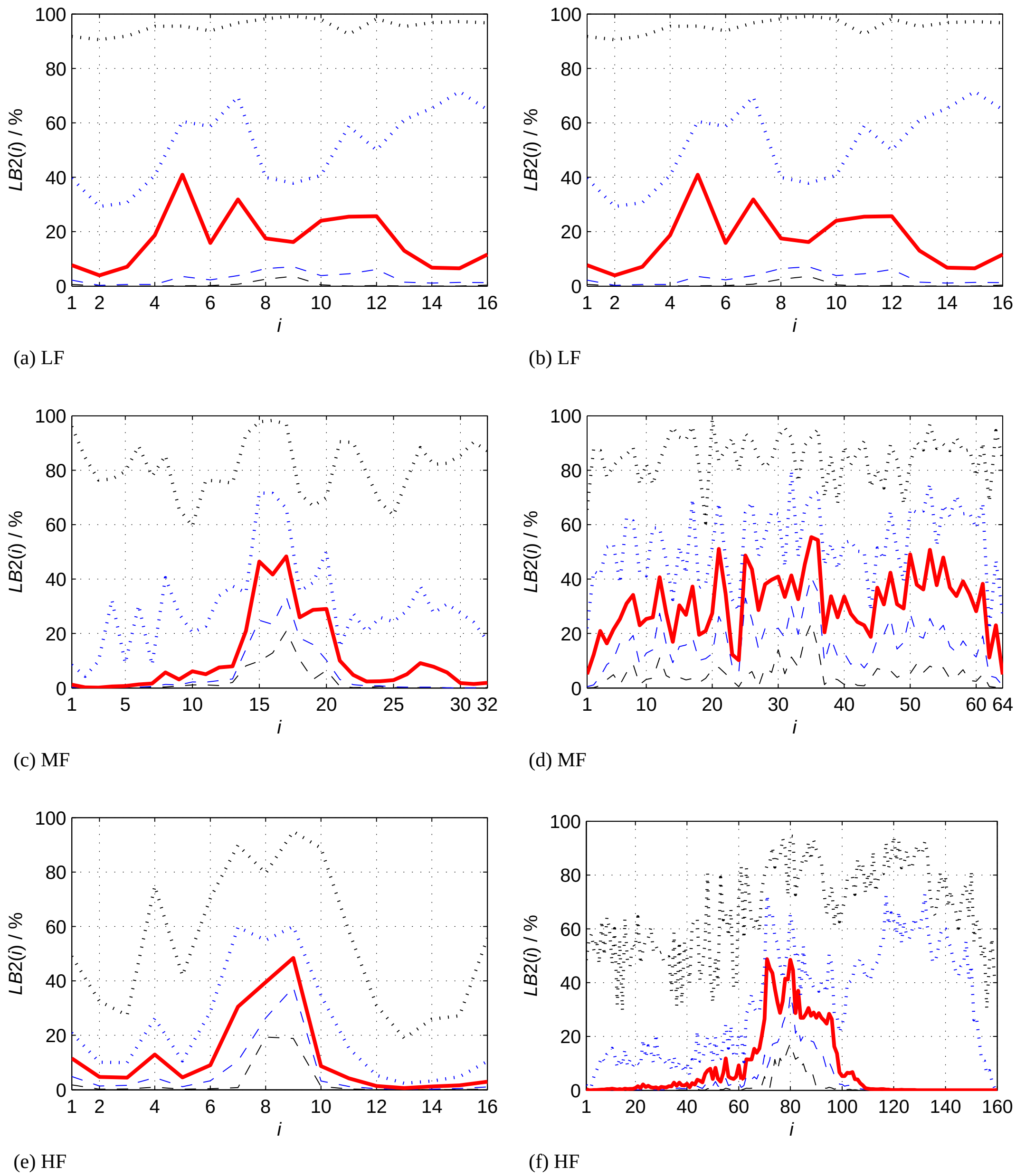

(a) LF (b) LF

(c) MF (d) MF

(e) HF (f) HF

Fig. 7: Evaluation plots for the LSA_1 (left) and the LSA_2 (right): source dependent load balancing $LB2(i)$, eq. (21), visualized separately for the low (LF), mid (MF) and high (HF) frequency range. Consider the legend in Fig. 6e that is valid for all depicted distribution measures.

trol effort [15, (3)], [16, (3)] in MZSFS and they quantitatively specify whether the individual sources are rather evenly or unevenly controlled. It could be possible that only few individual drivers are highly loaded whereas others are almost powered off. This should be avoided in practice due to loudspeaker and amplifier design and

symbol	item
$\varepsilon_{\text{abs}}(\omega)$	frequency dependent absolute error
$\varepsilon_{\text{rel}}(m,\omega)$	position and frequency dependent relative error
$L_{p,\text{a,na}}(\omega)$	relation of the obtained average sound pressure levels of the audience and the non-audience zone
$L_{p,\text{des,opt},q}(\omega)$	frequency dependent distribution measure of the level difference between the desired and the obtained sound field
$LB1(\omega)$	frequency dependent distribution measure of the drivers' load balancing with respect to the driver
$LB2(i)$	driver dependent distribution measure of the drivers' load balancing with respect to the frequency

Table 4: Overview of the proposed technical quality measures.

especially economical reasons. The first frequency dependent measure

$$LB1(\omega) = \frac{\underset{i}{\mathscr{Q}_q}\left[|D(i,\omega)|^2\right]}{\max\limits_i\left[|D(i,\omega)|^2\right]} \tag{20}$$

involves the calculation of the quantiles of the squared driving function weights with respect to all drivers i in relation to the maximum squared driving function weight for the respective frequency. Note that the squared driving function weights are proportional to the squared root mean square (RMS) voltage and are thereby proportional to the electrical power when assuming a real impedance. $LB1(\omega)$ is depicted in Fig. 6e and Fig. 6f.

Similarly, the outcome of the second proposed – source related – measure $LB2(i)$ are the quantiles with respect to the angular frequency ω in relation to the maximum squared driving function weight for the respective driver. Its equation is

$$LB2(i) = \frac{\underset{\omega}{\mathscr{Q}_q}\left[|D(i,\omega)|^2\right]}{\max\limits_\omega\left[|D(i,\omega)|^2\right]}. \tag{21}$$

This is visualized for the LF, MF and HF band of the two LWE-optimized LSAs in Fig. 7. In Tab. 4 an overview of the proposed technical quality measures is given.

6. DISCUSSION

The proposed visualizations and technical quality measures are discussed separately for the two LWE-optimized fictitious LSAs in this section.

6.1. Position Index Plots

As depicted in Fig. 3a and Fig. 3b the PIPs show acceptable optimization success with respect to the lowest frequencies for both considered LSAs. The LSA_2 provides a homogeneous sound field within the audience zone up to the spatial aliasing frequency of the HF band, whereas the LSA_1 produces aliasing within the MF and HF band since both exceed the allowed aliasing-free bandwidth. Due to insufficient audience coverage and severe corruption by spatial aliasing, the HF band of the LSA_1 synthesized sound field is unsuitable for sound reinforcement. Although WST-compliant the LSA_1 is not accessible for electronic control of the phase/ group delay in the HF band. Hence, only the magnitudes of the driving functions should be optimized, which is presumably approached in [6] to obtain satisfying results. Note that the WST criteria were derived for uniformly driven LSAs [10]. Only in this case large waveguides are appropriate post-filters to avoid or reduce spatial aliasing [11]. Both arrays exhibit an acceptable SPL reduction within the non-audience zones up to the spatial aliasing frequency.

6.2. Far-Field Radiation Patterns

The observations from the former sections can be confirmed by analyzing the FRPs in Fig. 3c and Fig. 3d. Moreover, they reveal a beam width of little larger than 45° for frequencies which the optimization performs at as intended. The beam width thus approximately matches the physical opening angle of the LSA spiral. For audience positions close to the LSA less power is required to produce the desired SPL. This can be traced back to the decreased level in the FRP at about $-60°$. The HF band of the LSA_1 exhibits a polar pattern that is similar to a uniformly driven, rectangular windowed LSA. This indicates that the optimization algorithm is not able to find a meaningful configuration other than that with least occurring spatial aliasing. A very narrow main lobe accompanied by side and grating lobes for frequencies larger than 1 kHz is obtained. The LSA_2 exhibits a more homogeneous polar pattern up to the spatial aliasing frequency in the HF band. At about 4 kHz aliasing artifacts begin to enter the LSA_2's visible region (i.e. $\pm 90°$). With increasing frequency those artifacts spread over a larger radiation angle range until finally entering the beam that is responsible for sound reinforcement of the audience zone. Hence, the sound field is severely corrupted within the audience and non-audience zones. The resulting frequency response coloration due to spatial aliasing plays a major role for the perceived sound quality, cf. [30, Fig. 5.10].

6.3. Sound Pressure Levels in the *xy*-plane

On the basis of the SPLxy plots in Fig. 9 and Fig. 10 analogue findings can be made as discussed above by means of the PIPs and FRPs. Especially the radiation behavior at very low and high frequencies with little optimization success due to the LSA characteristics should be taken into account (the LSA is too short for LF, the discretization Δy is too large for the highest frequencies). Referring to the LSA_2 Fig. 10e and Fig. 10f particularly give a vivid impression of the aliasing artifacts that corrupt the intended beam.

6.4. Driving Function Index Plots

In the DFIP plots (Fig. 4 for the LSA_1 and Fig. 5 for the LSA_2) the magnitude and group delay spectra for the individual LSA sources are shown for the LF, MF and HF band. A magnitude of 0 dB corresponds to the nominal driver sensitivity. This allows an estimation of the required power for the individual drivers. It leads to feasible results for the LF and HF band but not for the MF band with respect to the typical rated power load capacities of electrodynamic loudspeakers. Thus, the LSA modeling and the derived results must be seen as didactic design studies. As a general trend it can be stated that the LWE constraint causes an energy concentration in the middle of the LSA for the MF and HF band, whereas a more balanced load can be observed for the LF band. There are obvious differences in the MF band for $f < 800\,\mathrm{Hz}$ comparing the LSA_1 and the LSA_2. The DFIP of the LSA_1's HF band confirms the almost uniformly driven LSA only using the drivers in the middle of the array. Additionally, the delay does not change considerably above 5 kHz. Due to the high driving granularity of the LSA_2 the HF sources $i > 100$ are controlled in order to obtain the desired sound field for the very first audience positions. This works satisfactorily up to the spatial aliasing frequency. Regarding the 'system latency' due to the required FIR filters which is determined by the highest occurring group delays of the MF and HF band, the optimizations yield results which could be just used for live sound applications.

6.5. Sound Field Related Quality Measures

The measure $L_{p,\mathrm{a,na}}(\omega)$ (18) visualized in Fig. 6a and Fig. 6b reassures the preceding statements made with the help of the PIPs, FRPs and SPLxy. For the LF and MF band the averaged level difference is about 12 dB for the non-distance compensated case, i.e. the values are affected by the level decay due to the distance increase. Mainly differing from the first type in an offset and a drop for the lowest frequencies the respective level difference of the distance compensated version amounts to ca. 15 dB. This corresponds to the desired level difference of 20 dB reduced by the impact of the smooth transition between the audience and the non-audience zones. Beyond the spatial aliasing frequency $L_{p,\mathrm{a,na}}(\omega)$ strongly decreases after a peak for the LSA_1's MF and HF band at ca. 1.2 kHz and for the LSA_2's HF band at ca. 6 kHz. This measure misleadingly suggests a desirable high and increasing selectivity between the audience and non-audience zones in the LSA_1's HF band which is caused by the insufficient audience coverage.

By means of the distribution measure $L_{p,\mathrm{des,opt},q}(\omega)$ (19) that is depicted in Fig. 6c and Fig. 6d the general trends already stated above can be conveniently reviewed. A median near 0 dB and very little spread in the other quantiles are almost perfectly achieved from 1.5 kHz to 5 kHz for the LSA_2 indicating that a high LSA driving granularity leads to very good optimization results if the LSA length is much larger than the radiated wave length. Above the spatial aliasing frequency the spread increases exhibiting a non-symmetrical behavior. It can be noticed for the LSA_1 that a very high and unusable deviation and a spread arise in the HF band. For both LSAs the spread decreases with increasing frequency in the LF and MF band due to the varying 'wave length/ LSA length'-ratio. $L_{p,\mathrm{des,opt},q}(\omega)$ of the LSA_1's MF band evidently indicates by the increased spread the occurrence of spatial aliasing starting at about 1 kHz.

6.6. Source Related Quality Measures

The load balancing measure $LB1(\omega)$ in (20) that can be viewed in Fig. 6e and Fig. 6f shows that the individual sources are rather unevenly controlled, which can also be seen in the DFIPs. Only very few drivers provide the largest amount of the total energy in the HF band of the LSA_1. Interestingly, the median and the interquartile range (IQR) tend to become very small for frequencies above the spatial aliasing frequency, except some IQR-outliers in the HF band of the LSA_1. However, the large 0.95-quantile reveals that single drivers are loaded with very much power. Here the LSA_1 performs worse in the MF and HF band than the LSA_2.

A quantitative specification of the power distribution over the frequencies for each individual source can be pointed out by the $LB2(i)$ in (21) and is visualized in Fig. 7. As already observed the LF band is quite balanced, whereas the energy is concentrated in rather few sources referring to the HF band. In contrast to the LSA_1's MF band, the LSA_2's MF band exhibits a very balanced loading over the sources with respect to the individual frequencies.

7. CONCLUSION

By means of exemplarily performed optimizations of two modeled line source arrays several data visualizations are recollected and several technical measures are proposed in this paper. These are deployed in order to evaluate and interpret the technical quality of sound reinforcement. It is discussed that a full, in-depth and convenient interpretation of the observed phenomena is only possible when considering all the different graphical representation approaches in combination. This also prevents misinterpretation. The suggested technical measures may help to quantify the achieved optimization in terms of the sound field's and the driving functions' characteristics. The performed simulations unveil the common acoustic problems of spatial aliasing for high frequencies and insufficient beam forming capability for low frequencies. Spatial aliasing can be reduced by increasing the number of individually controlled drivers and decreasing the discretization step between them. Low frequency beam forming can be enhanced by using larger arrays. Since the performed evaluation is primarily intended as a design study introducing the strategies, it should be noted that other optimization algorithms may perform better, especially for the usage of line arrays with large waveguides. It is planned to incorporate the proposed technical quality measures as criteria for future optimization approaches. When using measured loudspeaker data it may be reasonable to include a further distribution measure for the required power and load balancing that relates the actual driving functions and the rated power. Analogue to the PIP magnitude data of the sound pressure, the corresponding phases should also be considered in the future in order to identify significant phase shifts that may affect the quality of auditory perception.

8. REFERENCES

[1] van Beuningen, G.W.J.; Start, E.W. (2000): "Optimizing directivity properties of DSP controlled loudspeaker arrays." In: *Proc. of the Inst. of Acoustics: Reproduced Sound*, **22**(6):17–37.

[2] Thompson, A. (2008): "Real world line array optimisation." In: *Proc. of the Institute of Acoustics*, **30**(6).

[3] Thompson, A. (2009): "Improved methods for controlling touring loudspeaker arrays." In: *Proc. of the 127th Audio Eng. Soc. Conv., New York*, #7828.

[4] Terrell, M.; Sandler, M. (2010): "Optimising the controls of a homogenous loudspeaker array." In: *Proc. of the 129th Audio Eng. Soc. Conv., San Francisco*, #8159.

[5] Thompson, A.; Baird, J.; Webb, B. (2011): "Numerically optimised touring loudspeaker arrays - Practical applications." In: *Proc. of the 131st Audio Eng. Soc. Conv., New York*, #8511.

[6] Feistel, S.; Sempf, M.; Köhler, K.; Schmalle, H. (2013): "Adapting loudspeaker array radiation to the venue using numerical optimization of FIR filters." In: *Proc. of the 135th Audio Eng. Soc. Conv., New York*, #8937.

[7] Thompson, A.; Luzarraga, J. (2013): "Drive granularity for straight and curved loudspeaker arrays." In: *Proc. of the Inst. of Acoustics*, **35**(2):210–218.

[8] Meyer Sound Laboratories Inc. (2002): "DSP beam steering with modern line arrays." Tech. rep., `https://www.meyersound.com/pdf/support/papers/beam_steering.pdf`, last seen on 2014-10-17.

[9] Feistel, S.; Thompson, A.; Ahnert, W. (2009): "Methods and limitations of line source simulation." In: *J. Audio Eng. Soc.*, **57**(6):379–402.

[10] Urban, M.; Heil, C.; Bauman, P. (2003): "Wavefront Sculpture Technology." In: *J. Audio Eng. Soc.*, **51**(10):912–932.

[11] Schultz, F.; Straube, F.; Spors, S. (2015): "Discussion of the Wavefront Sculpture Technology criteria for straight line arrays." In: *Proc. of the 138th Audio Eng. Soc. Conv., Warsaw*, #9323.

[12] Thompson, A. (2006): "Line array splay angle optimisation." In: *Proc. of the Inst. of Acoustics*, **28**(8):135–148.

[13] Choi, J.W.; Kim, Y.H. (2002): "Generation of an acoustically bright zone with an illuminated region using multiple sources." In: *J. Acoust. Soc. Am.*, **111**(4):1695–1700.

[14] Elliott, S.J.; Cheer, J.; Murfet, H.; Holland, K.R. (2010): "Minimally radiating sources for personal audio." In: *J. Acoust. Soc. Am.*, **128**(4):1721–1728.

[15] Coleman, P.; Jackson, P.J.B.; Olik, M.; Møller, M.; Olsen, M.; Pedersen, J.A. (2014): "Acoustic contrast, planarity and robustness of sound zone methods using a circular loudspeaker array." In: *J. Acoust. Soc. Am.*, **135**(4):1929–1940.

[16] Coleman, P.; Jackson, P.J.B.; Olik, M.; Pedersen, J.A. (2014): "Personal audio with a planar bright zone." In: *J. Acoust. Soc. Am.*, **136**(4):1725–1735.

[17] Bai, M.R.; Wen, J.C.; Hsu, H.; Hua, Y.H.; Hsieh, Y.H. (2014): "Investigation on the reproduction performance versus acoustic contrast control in sound field synthesis." In: *J. Acoust. Soc. Am.*, **136**(4):1591–1600.

[18] Cai, Y.; Wu, M.; Yang, J. (2014): "Sound reproduction in personal audio systems using the least-squares approach with acoustic contrast control constraint." In: *J. Acoust. Soc. Am.*, **135**(2):734–741.

[19] Meyer, D.G. (1984): "Computer simulation of loudspeaker directivity." In: *J. Audio Eng. Soc.*, **32**(5):294–315.

[20] Meyer, P.; Schwenke, R. (2003): "Comparison of the directional point source model and BEM model for arrayed loudspeakers." In: *Proc. of the Institute of Acoustics*, **25**(4).

[21] Schultz, F.; Rettberg, T.; Spors, S. (2014): "On spatial-aliasing-free sound field reproduction using finite length line source arrays." In: *Proc. of the 137th Audio Eng. Soc. Conv., Los Angeles*, #9098.

[22] Skudrzyk, E. (1971): *The Foundations of Acoustics*. New York: Springer.

[23] Olver, F.W.J.; Lozier, D.W.; Boisvert, R.F.; Clark, C.W. (2010): *NIST Handbook of Mathematical Functions*. Cambridge University Press, 1. ed.

[24] Heil, C.; Urban, M. (1992): "Sound fields radiated by multiple sound sources arrays." In: *Proc. of 92nd Audio Eng. Soc. Conv., Vienna*, #3269.

[25] Deschamps, G.A.; Cabayan, H.S. (1972): "Antenna synthesis and solution of inverse problems by regularization methods." In: *IEEE Trans. on Antennas and Propagation*, **20**(3):268–274.

[26] Nelson, P.A. (2001): "A review of some inverse problems in acoustics." In: *J. Acoust. and Vibr.*, **6**(3):118–134.

[27] Kim, Y.; Nelson, P. (2004): "Optimal regularisation for acoustic source reconstruction by inverse methods." In: *J. of Snd. Vibr.*, **275**(3):463–487.

[28] Betlehem, T.; Withers, C. (2012): "Sound field reproduction with energy constraint on loudspeaker weights." In: *IEEE Trans. on Audio, Speech, and Language Processing*, **20**(8):2388–2392.

[29] Ahrens, J.; Spors, S. (2010): "Sound field reproduction using planar and linear arrays of loudspeakers." In: *IEEE Trans. Audio Speech Language Process.*, **18**(8):2038–2050.

[30] Wierstorf, H. (2014): *Perceptual assessment of sound field synthesis*. Ph.D. thesis, TU Berlin.

[31] Malyshev, A.N. (2003): "A unified theory of conditioning for linear least squares and Tikhonov regularization methods." In: *SIAM J. Matrix Anal. Appl.*, **24**(4):1186–1196.

9. APPENDIX

LSA cabinet	γ_n / deg	$x_{c,n}$ / m	$y_{c,n}$ / m
1	-3	0.0097	2.8143
2	-1	0.0227	2.4425
3	1	0.0227	2.0706
4	3	0.0097	1.6989
5	5	-0.0162	1.3278
6	7	-0.0551	0.9579
7	10	-0.1101	0.5901
8	12	-0.1810	0.2250
9	15	-0.2678	-0.1366
10	18	-0.3735	-0.4931
11	21	-0.4976	-0.8437
12	24	-0.6399	-1.1872
13	27	-0.8000	-1.5229
14	30	-0.9774	-1.8497
15	34	-1.1744	-2.1650
16	38	-1.3930	-2.4657

Table 5: Front grille center positions and tilting angles of the LSA cabinets for the geometry used in Fig. 1.

m	x_m / m	y_m / m
1	0	-11
1 401	7	-11
10 001	50	-11
12 063	58.0017	-4.4986
13 062	58.0017	0.4964
15 124	66.0035	6.9978
16 325	66.0035	13.0028
29 525	0.0035	13.0028

Table 6: Selected venue slice coordinates according to Fig. 2.

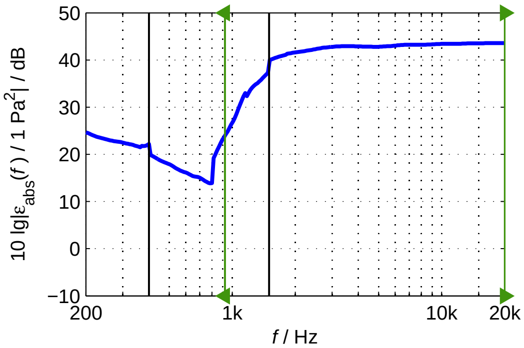

(a) $\varepsilon_{\mathrm{abs}}(\omega)$

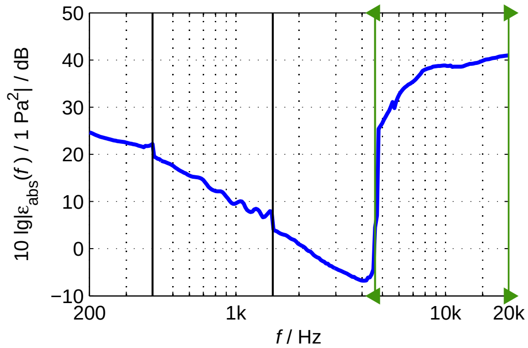

(b) $\varepsilon_{\mathrm{abs}}(\omega)$

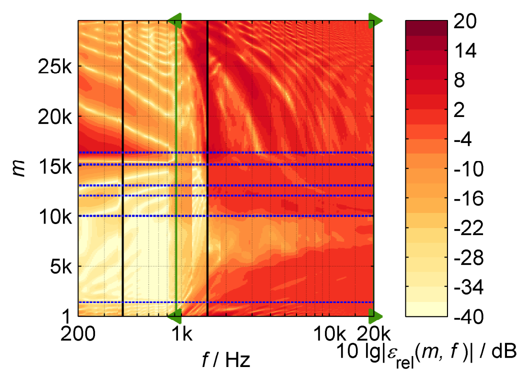

(c) $\varepsilon_{\mathrm{rel}}(m,\omega)$

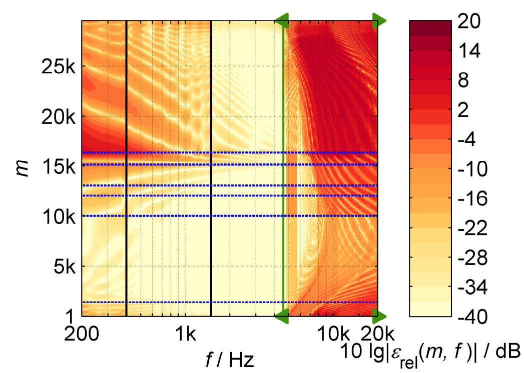

(d) $\varepsilon_{\mathrm{rel}}(m,\omega)$

Fig. 8: Evaluation plots for the LSA$_1$ (left) and the LSA$_2$ (right), top: frequency dependent absolute error $\varepsilon_{\mathrm{abs}}(\omega)$, eq. (16), bottom: position and frequency dependent relative error $\varepsilon_{\mathrm{rel}}(m,\omega)$, eq. (17). The crossover frequencies (black) and the spatial aliasing frequencies of straight arrays (green with arrows) according to Tab. 2 are charted for orientation.

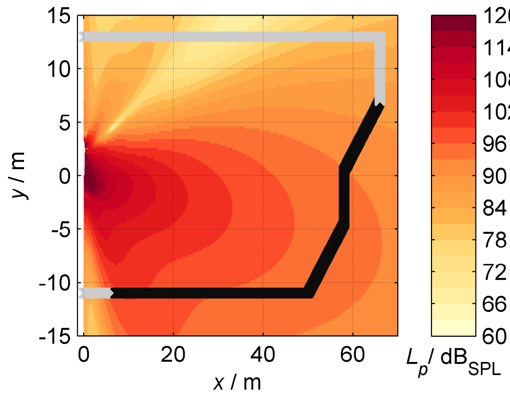

(a) $f = 200$ Hz

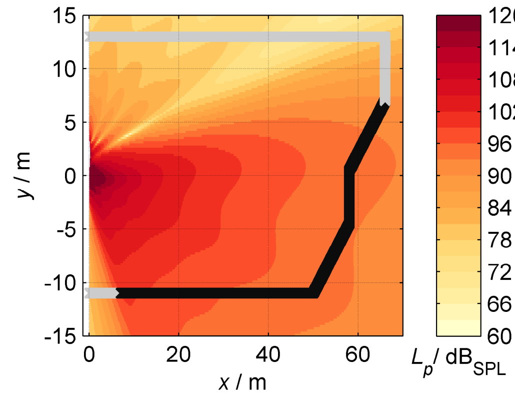

(b) $f = 500$ Hz

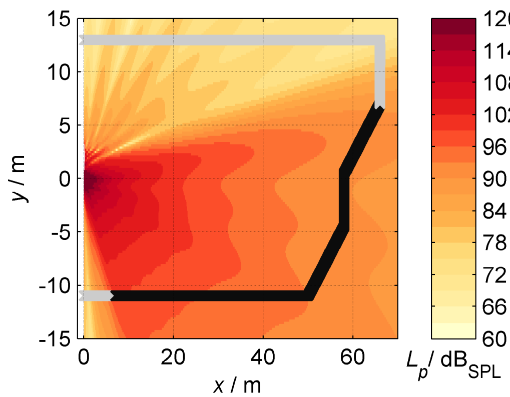

(c) $f = 1$ kHz

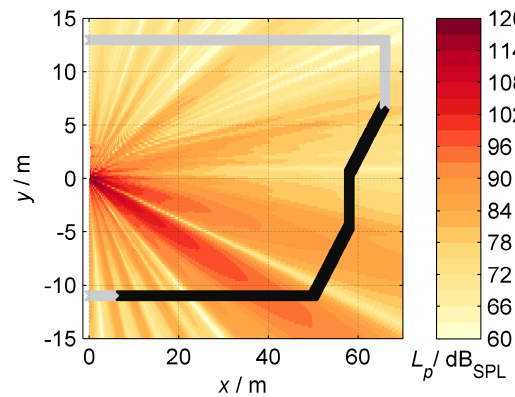

(d) $f = 5$ kHz

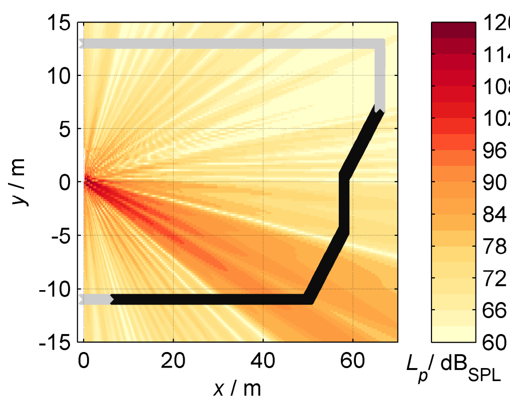

(e) $f = 10$ kHz

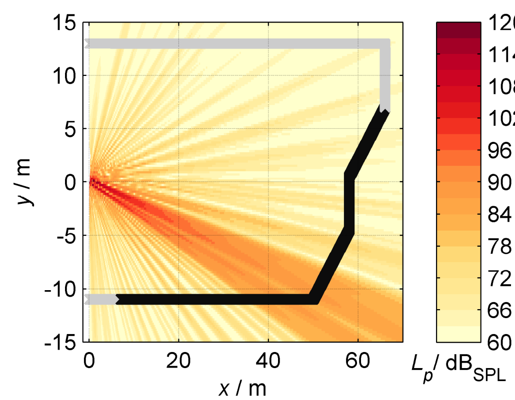

(f) $f = 16$ kHz

Fig. 9: Sound pressure levels in the *xy*-plane (SPLxy) for the LWE-optimized LSA_1. Optimized for the position index plot points.

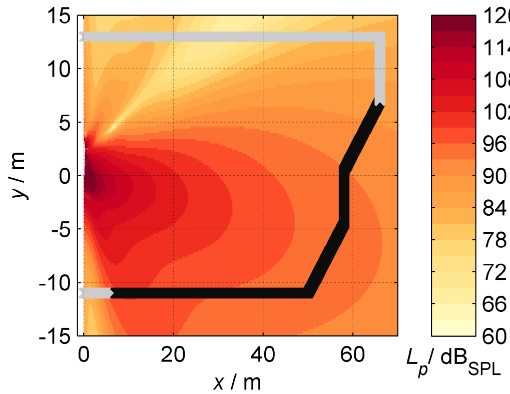

(a) $f = 200$ Hz

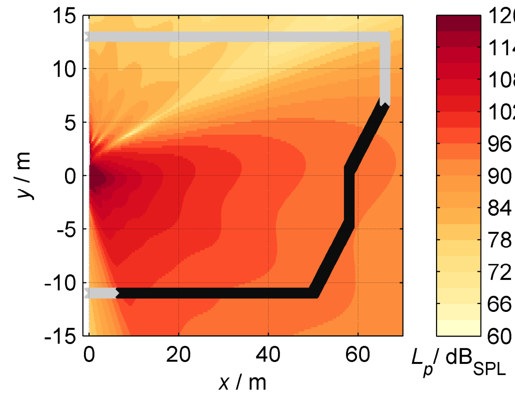

(b) $f = 500$ Hz

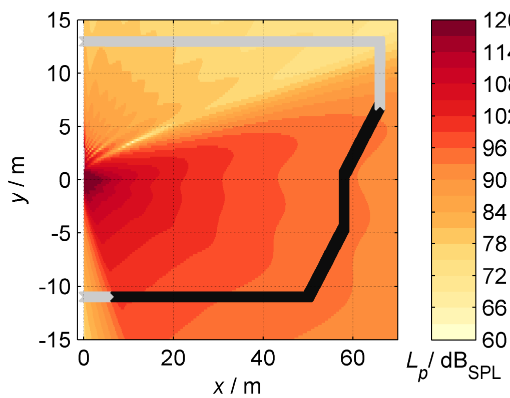

(c) $f = 1$ kHz

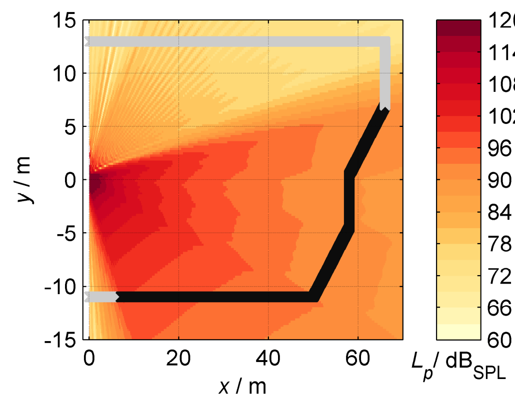

(d) $f = 5$ kHz

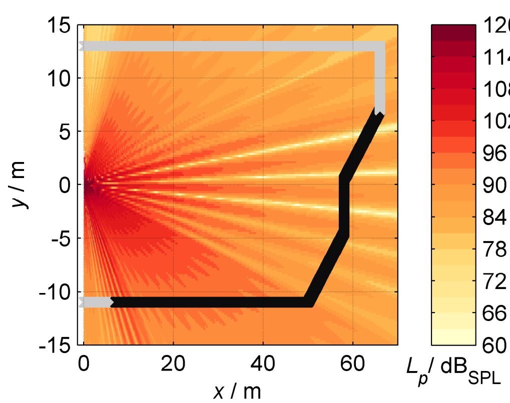

(e) $f = 10$ kHz

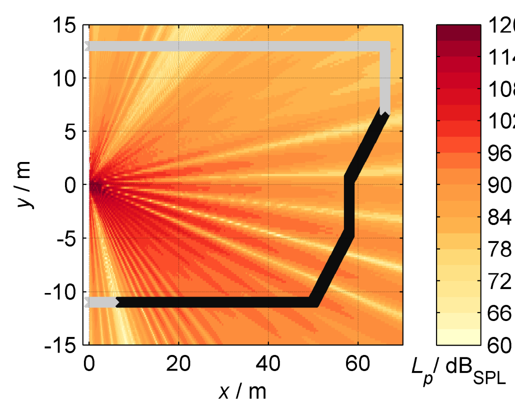

(f) $f = 16$ kHz

Fig. 10: Sound pressure levels in the *xy*-plane (SPLxy) for the LWE-optimized LSA_2. Optimized for the position index plot points.

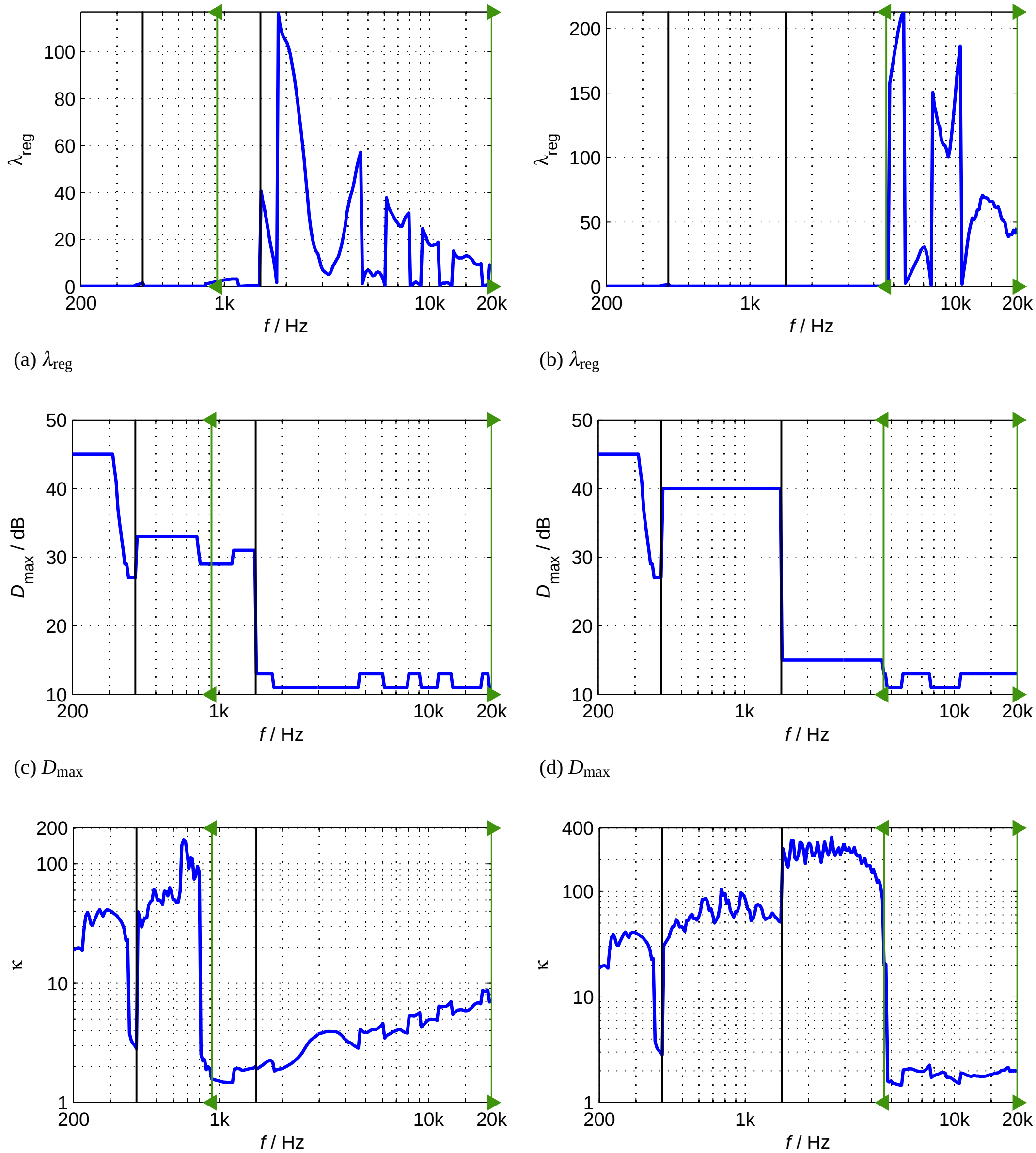

(a) λ_{reg} (b) λ_{reg}

(c) $D_{\max}$ (d) $D_{\max}$

(e) κ (f) κ

Fig. 11: Optimization parameters for the LSA$_1$ (left) and the LSA$_2$ (right), top: regularization parameter λ_{reg}, mid: $D_{\max}$, bottom: condition number κ for the Tikhonov regularized solution, cf. [26], [31, (3.1b)]. The crossover frequencies (black) and the spatial aliasing frequencies of straight arrays (green with arrows) according to Tab. 2 are charted for orientation.